

Observation of photon recoil effects in single-beam absorption spectroscopy with an ultracold strontium gas

Fachao Hu,^{1,2,*} Canzhu Tan,^{1,2,*} Yuhai Jiang,^{3,2,†} Matthias Weidemüller,^{1,2,4,‡} and Bing Zhu^{4,2,§}

¹*Hefei National Laboratory for Physical Sciences at the Microscale,
University of Science and Technology of China, Hefei, Anhui 230026, China*

²*CAS Center For Excellence in Quantum Information and Quantum Physics,
University of Science and Technology of China, Hefei, Anhui 230026, China*

³*Shanghai Advanced Research Institute, Chinese Academy of Sciences, Shanghai 201210, China*

⁴*Physikalisches Institut, Universität Heidelberg, Im Neuenheimer Feld 226, 69120 Heidelberg, Germany*

(Dated: January 19, 2022)

We report on observing photon recoil effects in the absorption of a single monochromatic light at 689 nm through an ultracold ^{88}Sr gas, where the recoil frequency is comparable to natural linewidth of the narrow-line transition $5s^2\ ^1\text{S}_0 - 5s5p\ ^3\text{P}_1$ in strontium. In the regime of high-saturation, the absorption profile becomes asymmetric due to the photon-recoil shift, which is of the same order as the natural linewidth. The lineshape is described by an extension of the optical Bloch equations including the momentum transfers to atoms during emission and absorption of photons. Our work reveals the photon recoil effects in a simplest single-beam absorption setting, which is of significant relevance to other applications such as saturation spectroscopy, Ramsey interferometry, and absorption imaging.

I. INTRODUCTION

When emitting or absorbing a photon, the motional degree of freedom of an atom is modified due to the so-called photon recoil effect, which is well-known and has triggered major breakthroughs in modern atomic physics through the developments of laser cooling and trapping techniques [1]. This effect also arises special interests in atomic spectroscopy [2] and interferometry [3], single-photon scattering on a motional scatter [4], and collective and cooperative light scattering in atom arrays for quantum information or control of light [5, 6].

The study of photon recoil effects on atomic spectra dates back to 1970s in the context of laser technology and precision measurements [7]. Three different frequencies are important when considering such an effect for an ensemble of two-level atoms irradiated by a monochromatic light, namely the natural linewidth of the atomic transition Γ , the recoil frequency $\gamma = \hbar k^2/2m$, and the Doppler shift kv_0 . Here \hbar is the reduced Planck constant, $k = 2\pi/\lambda$ is the light wavenumber (λ the light wavelength), m is the atomic mass, and v_0 is the most probable velocity in the atomic ensemble. In case that $\Gamma \gg \gamma, kv_0$, the photon recoil can manifest itself in the effects of recoil-induced resonances ($kv_0 \gg \gamma$) [8, 9] and the collective atomic recoil laser ($kv_0 \lesssim \gamma$) [10, 11]. When γ becomes comparable to or even larger than Γ , the photon recoil effects can cause a splitting in saturation spectroscopy, which was first predicted more than 60 years ago [2] and demonstrated in various experiments [12–

15]. The cumulative recoils lead to spontaneous scattering force, as studied also by saturation spectroscopy in Refs. [16–22], although all the studies were performed with at least two laser beams for heated vapor gases or fast atomic beams and Γ is still considerably larger than γ .

In this work, we show the photon-recoil-induced asymmetry and shift in the absorption profile on the narrow-line transition $5s^2\ ^1\text{S}_0 - 5s5p\ ^3\text{P}_1$ at 689 nm with an ultracold ^{88}Sr atomic cloud, where $\Gamma/2\pi = 7.5$ kHz, $kv_0/2\pi \sim 24$ kHz, and $\gamma/2\pi = 4.8$ kHz. By monitoring the transmission of a single monochromatic beam through an ultracold dilute strontium gas (the atomic density $n \sim 8.9 \times 10^{10}$ cm $^{-3}$), we observe asymmetrical and shifted spectra depending nonlinearly on the light intensity. The simple experimental configuration studied here allows us to compare the measurements quantitatively to a theoretical simulation based on optical Bloch equations (OBEs) involving the momentum transfers during the photon absorption and emission processes. Although the photon recoil effect was investigated extensively for $\gamma \lesssim \Gamma$ starting from more than four decades ago [12–15], all the studies involved complex beam configurations like saturation or Ramsey spectroscopic and it has been elusive for observing corresponding phenomena using a single-beam setup. This work will be relevant to high-resolution optical spectroscopy with strontium or other alkali-earth (like) systems [23–27].

The article is organized as follows: We show our experimental setup in Sec. II. The observation of photon recoil effects in the absorption spectra are described in Sec. III and the theoretical simulation and comparison to experiments are discussed in Sec. IV. Sec. V concludes the paper.

* These authors contributed equally to this work.

† jiangyh@sari.ac.cn

‡ weidemueller@uni-heidelberg.de

§ bzh@physi.uni-heidelberg.de

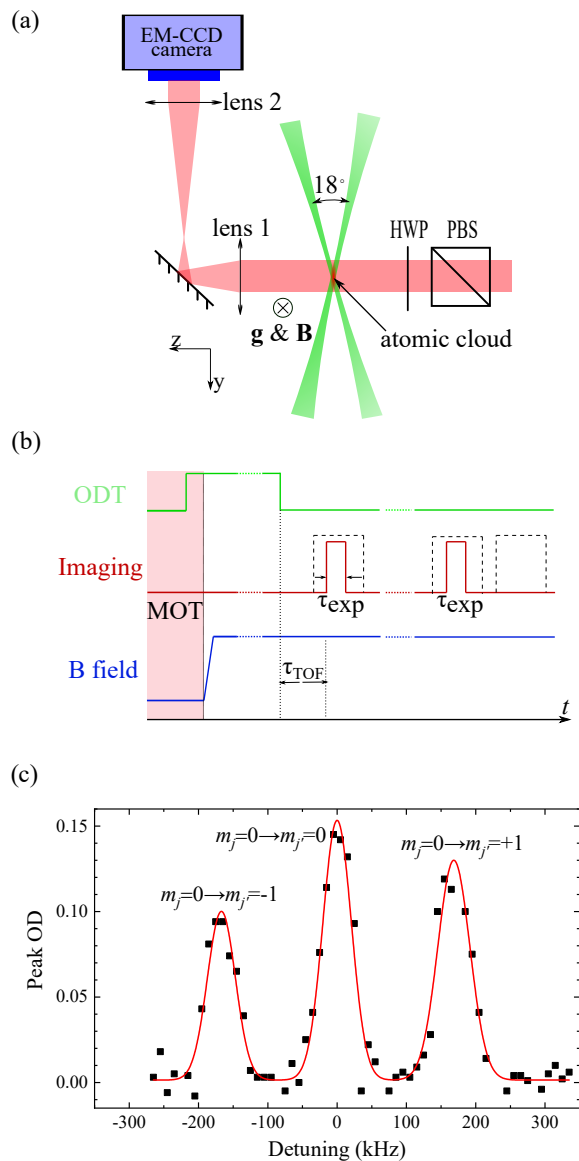


FIG. 1. (a) Schematic of the top view of experimental setup. HWP: half wave-plate; PBS: polarizing beam-splitter. \mathbf{g} and \mathbf{B} represent the gravity and magnetic field, respectively. See text for more details. (b) Time sequence for absorption spectroscopy. See text for explanations of τ_{TOF} and τ_{exp} . (c) Absorption spectrum showing all three Zeeman sublevels of $^3\text{P}_1$ state when the probe light polarization is tuned to about 45° angled to the residual magnetic field. Black points are the measured peak OD, and the red curve is the fit to a multi-peak Gaussian function. The obtained Zeeman splitting is $167.7(1.2)$ kHz, corresponding to a magnetic field of $79.9(6)$ mG.

II. EXPERIMENTAL SETUP

Fig. 1(a) shows the experimental setup. The ^{88}Sr atoms are first loaded into a two-stage magneto-optical trap (MOT) for the laser cooling and trapping [28, 29], operated on the broad $5s^2\ ^1\text{S}_0 - 5s5p\ ^1\text{P}_1$ and narrow

$5s^2\ ^1\text{S}_0 - 5s5p\ ^3\text{P}_1$ transitions, respectively. Typically we produce an atomic cloud of 10^6 atoms with a density of about $10^{10}\ \text{cm}^{-3}$ and a temperature around $1\ \mu\text{K}$ in the MOT. A cigar-shaped optical dipole trap (ODT) formed by two horizontally propagating beams at the wavelength of $532\ \text{nm}$, is simultaneously switched on during the narrow-line MOT [29]. The two ODT beams both have a waist of about $60\ \mu\text{m}$ and cross at an angle of 18° . Holding atoms in the ODT for $200\ \text{ms}$ to reach equilibrium after switching off the MOT, we obtain about $(0.5 \cdots 5) \times 10^5$ atoms at a temperature of $0.7 \cdots 6\ \mu\text{K}$ depending on the ODT power. At a power of $0.6\ \text{W}$ for each beam the trap depth of the ODT is about $6\ \mu\text{K}$ and the trap frequencies are $2\pi \times (217, 34, 217)$ Hz along the x , y , and z directions [see Fig. 1(a)], respectively, resulting in cloud radii of $(27, 69, 27)\ \mu\text{m}$ and a peak density of $7 \times 10^{11}\ \text{cm}^{-3}$. The above-mentioned atom numbers, cloud sizes, and temperatures are measured using standard time-of-flight (TOF) imaging technique [30] with the broad $5s^2\ ^1\text{S}_0 - 5s5p\ ^1\text{P}_1$ transition ($\Gamma/2\pi \approx 32\ \text{MHz}$). The lifetime of the atomic clouds in the ODT is about $2\ \text{s}$, limited by the collisions with background particles.

The probe light at $689\ \text{nm}$ is delivered from a commercial tapered amplifier seeded by an external-cavity diode laser (Toptica TApro), used also for the narrow-line MOT cooling, which is frequency-stabilized to a passive ultra-low expansion cavity with a short-term noise of $1\ \text{kHz}$ level and a long-term drift of $8\ \text{kHz/day}$ [29]. As shown in Fig. 1(a), the probe beam propagates along the z direction with a tunable linear polarization and has a $1/e^2$ diameter of $4.2\ \text{mm}$. The probe pulse length and intensity are controlled by an acousto-optic modulator (not shown in the figure). The intensity distribution of the transmitted probe light is mapped out after passing two achromatic lenses with focal lengths of $+200\ \text{mm}$ and $+300\ \text{mm}$ by an EM-CCD camera from Andor, resulting in a resolution of about $12\ \mu\text{m}$ [see Fig. 1(a)].

The experimental sequence is described in Fig. 1(b). The absorption spectroscopy is performed after rapidly switching off the ODT to avoid the differential AC Stark shifts on the energy levels. A quantization magnetic field along the vertical direction is imposed (rising time $2\ \text{ms}$) before the probe pulse to split the Zeeman sublevels of $^3\text{P}_1$, as seen in Fig. 1(b). After a given TOF time τ_{TOF} , the atoms are shined by the probe light with an exposure time $\tau_{\text{exp}} = 200\ \mu\text{s}$. By tuning the τ_{TOF} we can tune the atomic density during the absorption, which is important to avoid the dispersive lensing effect (see Appendix B). τ_{TOF} is fixed to $3.1\ \text{ms}$ if not specified explicitly. Two additional images with and without the probe light are taken after the first absorption pulse and the three images are then processed (see, e.g., [31]) to obtain the so-called two-dimensional optical density (OD) distribution of the atomic cloud [see the insets of Fig. 2(b,c,d)], as done for the standard absorption imaging of ultracold atomic gases [30].

By changing the linear probe polarization angle in the $x - y$ plane, all three Zeeman sublevels of the $^3\text{P}_1$ state

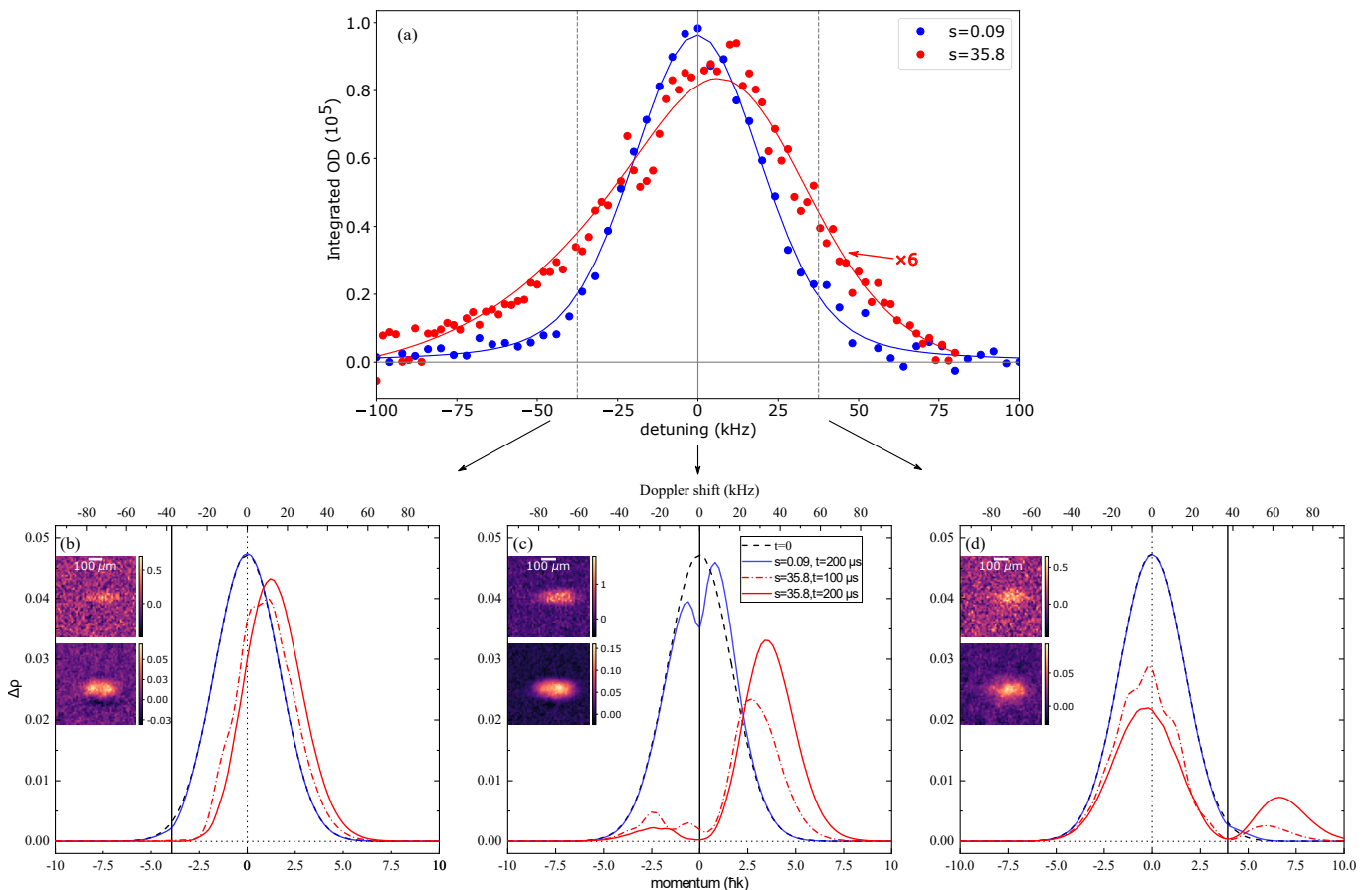


FIG. 2. Photon recoil effects. (a) The measured absorption lineshapes at low (blue dots) and high (red dots) saturations. The data in the high-saturation case ($s = 35.8$) showing asymmetric profile is fitted to the numerical solution of Eq. (4) (red curve) and magnified by 6 times to have a better visualization. As a comparison, the low-saturation ($s = 0.09$) data is symmetric and fits well to the Voigt profile (blue curve). (b) - (d), the population difference $\Delta\rho_\delta(p)$ obtained from the OBE solutions at there different detunings [$0, \pm 5\Gamma$, as marked by the grey vertical lines in (a)] after an exposure time of $100\ \mu\text{s}$ and $200\ \mu\text{s}$, respectively. As a reference, we also show the initial distribution at $\tau_{\text{exp}} = 0$, which is the Maxwell-Boltzmann one determined by the cloud temperature. The black solid vertical lines mark the resonant momentum positions, where the probe detuning is compensated by the Doppler effect. The inset images show measurements of the two-dimensional OD distributions at low (upper) and high (lower) saturations for their respective detunings.

are observable. An example is shown in Fig. 1(c). The peak OD is measured as a function of the probe detuning showing three peaks at a magnetic field of about 80 mG. The relative line strengths are determined by the polarization and the different coupling strengths of the three corresponding transitions (see Fig. 1(c)). We have used this measurement to optimize the compensation of the background magnetic field to be better than 5 mG in our setup and to calibrate the quantization fields. For the absorption spectroscopy discussed below, we apply a field of 4 G to split the sublevels of $^3\text{P}_1$ further (~ 8 MHz) and the probe polarization is tuned parallel to the quantization axis, so that the system is subjected only to the closed π transition ($m_j = 0 \rightarrow m_{j'} = 0$), which can be treated as a perfect two-level system.

III. MEASUREMENTS

Thanks to the high sensitivity and large dynamical range of our imaging camera (Andor iXon 897) at 689 nm, we can study the absorption spectrum on the narrow-line transition with a saturation parameter s ranging from 0.01 to more than 100. Here $s = I/I_s$ is the ratio between probe intensity I and the saturation intensity $I_s = 3\ \mu\text{W}/\text{cm}^2$. Here we will focus on the narrow-line absorption spectrum at strong saturations with $s \gg 1$. Naturally, one would expect more photon recoil events for longer probe time τ_{exp} . However, the signal-to-noise ratio (SNR) is already strongly suppressed for $\tau_{\text{exp}} > 300\ \mu\text{s}$ in our measurements (explained later). We chose $\tau_{\text{exp}} \geq 100\ \mu\text{s} \sim 5/\Gamma$ to ensure an observable recoil effect and $\tau_{\text{exp}} \leq 250\ \mu\text{s}$ for a large enough SNR.

In Fig. 2(a) we compare two absorption spectra with $\tau_{\text{exp}} = 200 \mu\text{s}$ at saturation parameters of $s = 0.09$ (blue points) and $s = 35.8$ (red points), respectively. Instead of the peak OD, the integrated one over the whole atomic cloud region is shown, which is to be compared with the OBE solutions including contributions from all atoms of different velocities (see Sec. IV). The low-saturation data shows a symmetric, zero-centered profile, which can be described very well by a Gaussian function with a width determined by the cloud temperature (see Appendix A). At high saturation, we observe a decrease of the integrated OD signal at all detunings due to the saturation effect (note that the data at higher saturation is magnified by a factor of 6 for a better view). Here the integrated OD refers to the sum of all the measured ODs in the atomic cloud region. More importantly, the lineshape is asymmetric at the high saturation, namely the integrated OD approaches zero more slowly on the negative-detuning side than that on the positive one, and the absorption peak is shifted by a few kHz to the positive detuning. At high saturation, differences can already be seen in the OD images at the two detuning sides [see lower rows in the insets of Figs. 2(b-d)], namely a wider spatial extension for the positive detuning than that for the negative one. In this series of experiments, the influence of the lensing effect on the OD measurement (see Appendix B) is negligible due to the low atomic densities involved here.

The observed asymmetry and peak shift can be interpreted qualitatively by considering the absorption process including the influence of the photon recoil. The photon recoil associated with each absorption-spontaneous emission cycle redistributes the momentum of atoms, which depends strongly on the light detuning [32]. Consequently, an asymmetric lineshape and the shift of the maximum of absorption emerges when more and more photons are scattered due to the momentum redistribution in the atomic cloud. In order to resolve such effects, the Doppler width has to be comparable to the power-broadened line width. In the case of the strong saturation in Fig. 2(a), the power-broadened Lorentzian width $\Gamma\sqrt{1+s} \sim 45 \text{ kHz}$ is close to the Doppler one of $\sim 40 \text{ kHz}$. In the following subsection a quantitative description is presented incorporating the photon-recoil effect in an OBE formalism.

IV. SPECTRUM LINESHAPE SIMULATION

We take an OBE formalism including the method of so-called 'momentum families' from Ref. [33], originally developed to understand laser cooling on a narrow-line transition. The model considers a two-level atom system with an initial Maxwell-Boltzmann thermal distribution, interacting with a single near-resonant monochromatic homogeneous probe beam. The state of an atom with momentum \mathbf{p} is expressed in the form of $\{|g, \mathbf{p}\rangle, |e, \mathbf{p}\rangle\}$, where $|g(e)\rangle$ corresponds to the atomic ground (excited)

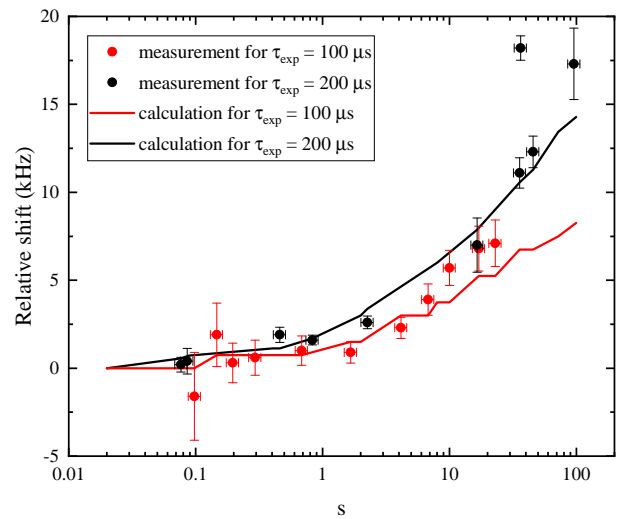


FIG. 3. Absorption peak position shift. The relative position of the absorption peak at different saturation parameters s are compared for imaging times of $100 \mu\text{s}$ (red circles and curve) and $200 \mu\text{s}$ (black circles and curve). The black and red curves are the calculated results without any free parameters, while the black and red circles are the fitted results from measurements by using the peak position and height as the two free fitting parameters. The error bars for the horizontal axis come mainly from uncertainties of measuring the probe power and those for the vertical axis are from fitting. See text for more discussions.

state. The system Hamiltonian driven under a laser beam propagating along the z axis is,

$$H_0 = \frac{\hat{p}^2}{2m} + \hbar\omega_0 |e\rangle \langle e| - \hat{\mathbf{D}} \cdot \hat{\mathbf{E}} \quad (1)$$

where $\omega_0, \hat{\mathbf{D}}, \hat{\mathbf{E}}$ are the transition frequency, dipole moment operator, and laser electric field, respectively. In our case, only the π -transition branch $m_j = 0 \rightarrow m_{j'} = 0$ is considered, and only momentum along the light propagation axis $p = p_z$ is preserved, with the other two components p_x, p_y traced over. The system Hamiltonian under the rotating-wave approximation becomes,

$$H_S = \frac{\hat{p}^2}{2m} - \hbar\delta |e\rangle \langle e| + \frac{\hbar\Omega}{2} (e^{ikz} |e\rangle \langle g| + |g\rangle \langle e| e^{-ikz}) \quad (2)$$

where δ, Ω are the bare detuning and Rabi frequency.

The evolution of states $|g, p\rangle, |e, p + \hbar k\rangle$ with any momentum p remains globally closed under H_S when the spontaneous emission is not considered, for which reason the states $|g, p\rangle, |e, p + \hbar k\rangle$ are grouped as a family $\mathcal{F}(p)$. The system density matrix ρ expanded in this basis is,

$$\begin{aligned} \rho_{gg}(p) &= \langle g, p | \rho | g, p \rangle \\ \rho_{ee}(p) &= \langle e, p + \hbar k | \rho | e, p + \hbar k \rangle \\ \rho_{ge}(p) &= \rho_{eg}^*(p) = \langle g, p | \rho | e, p + \hbar k \rangle \end{aligned} \quad (3)$$

The equations of evolution under H_S together with the

spontaneous emission processes are,

$$\begin{aligned}
\dot{\rho}_{gg}(p) &= \Gamma \bar{\pi}_e(p - \hbar k) - \frac{i\Omega}{2}(\rho_{eg}(p) - \rho_{ge}(p)), \\
\dot{\rho}_{ee}(p) &= -\Gamma \bar{\pi}_e(p) + \frac{i\Omega}{2}(\rho_{eg}(p) - \rho_{ge}(p)), \\
\dot{\rho}_{ge}(p) &= \dot{\rho}_{eg}^*(p) \\
&= -(i(\bar{\delta} - \frac{kp}{m}) + \frac{\Gamma}{2})\rho_{ge}(p) + \frac{i\Omega}{2}(\rho_{gg}(p) - \rho_{ee}(p)),
\end{aligned} \tag{4}$$

where $\bar{\delta} = \delta - \hbar k^2/(2m)$ and the term $\bar{\pi}_e$ represents the impact of spontaneous decay on the system evolution, defined as

$$\begin{aligned}
\bar{\pi}_e(p) &= \int_{-\infty}^{+\infty} dp_x \int_{-\infty}^{+\infty} dp_y \int_{-\hbar k}^{+\hbar k} dp' \mathcal{N}(p') \\
&\langle e, p_x, p_y, p_z = p + p' | \rho | e, p_x, p_y, p_z = p + p' \rangle.
\end{aligned} \tag{5}$$

Here $\mathcal{N}(p') = \frac{3}{4\hbar k}(1 - p'^2/\hbar^2 k^2)$ results from the classical dipole radiation pattern [33] of the π transition. With all the atoms initially at the ground state $|g\rangle$ with a Maxwell-Boltzmann distribution of temperature T , we numerically integrate the equations (4) to get the system evolution. The solution of the off-diagonal elements $\rho_{eg}(p)$ results in the susceptibility $\chi(p) \propto n\rho_{eg}(p)$ with the atomic density n . The absorption profile is then calculated by tracing the imaginary part of the susceptibility over all momenta, i.e. $\sum_p \text{Im}\chi(p)$, and then integrating over the interaction duration.

For the solid curves in Figs. 2(a), we fit the experimental data to the calculated profiles with the maximum integrated OD and the peak position as the only free parameters. Both the lineshape asymmetry and the shift of the absorption peak at high saturation can be reproduced very well by Eq. (4) including the momentum transfer due to the photon-scattering events. While the model predicts a significant shift of the absorption peak, its position is still used as a free parameter in the fits to account for the possible deviation between the measurements and the calculations, as discussed in more details later in Fig. 3.

One can gain further insight into the observed photon-recoil effects by considering the detuning-dependent distribution of the susceptibility in the momentum space, the imaginary part of which accounts for the absorption and reads $\text{Im}\chi_\delta(p) \propto \frac{\Delta\rho_\delta(p)}{\Gamma/\Omega + (\delta/\Omega - kp/m\Omega)^2}$ in the quasi-steady solution of Eq. (4). Here $\Delta\rho_\delta(p) = \rho_{gg}(p) - \rho_{ee}(p)$ represents the population difference between the ground and excited states at a detuning δ for atoms with a momentum between p and $p + dp$ such that $\int[\rho_{gg}(p) + \rho_{ee}(p)]dp = 1$. If the photon recoils can be neglected, the integration of $\text{Im}\chi(\delta, p)$ over the momentum space results in a symmetric absorption profile with respect to the detuning δ . At all detunings the initial distribution is Gaussian determined by the gas temperature. In general, the momentum transferred to atoms during

the photon scattering would reduce the absorption due to the parabolic dependence on p in the denominator of $\text{Im}\chi_\delta(p)$, and hence reducing the SNR for stronger recoils.

We show from Fig. 2(b) to 2(d) the calculated distribution of the population difference $\Delta\rho_{-5\Gamma,0,+5\Gamma}(p)$ in the momentum space at two saturation parameters of $s \approx 0.09$ (blue curves) and $s = 35.8$ (red curves) after 200- μs atom-light interaction time ($\tau_{\text{exp}} \sim 10/\Gamma$ to ensure a quasi-steady state condition), respectively. At the low saturation ($s \approx 0.09$), this distribution at all three δ is only slightly modified if compared to the initial Maxwell-Boltzmann distribution (black dot-dashed lines), remaining almost Gaussian even after long interaction time. This behaviour agrees with a weak photon-recoil effect and results in a lineshape nearly the Voigt one, as the blue curve seen in Fig. 2(a). When highly saturated ($s = 35.8$), however, the $\Delta\rho(p)$ distribution is strongly affected and we observe a significant depletion of atoms near the resonant momentum (marked by vertical dashed lines), where the Doppler shift compensates the bare imaging detuning. In Fig. 2(b) with a detuning of -5Γ , the distribution maintains a Gaussian shape with the center shifted by $\sim 1.2\hbar k$ after 200 μs . While at a detuning of $+5\Gamma$ in Fig. 2(d), two peaks appear on the opposite sides of the resonant momentum. Such a strong dependence on the detuning results from the fact that the probe light constantly transfers a positive momentum to the atomic ensemble and this transfer is highly momentum dependent for a narrow transition. We further note that to observe the asymmetric lineshape and the peak shift one would need also low sample temperatures to ensure the visibility of the momentum transfer effect.

The effects of the photon recoil can also be revealed by studying the time evolution of the momentum distribution $\Delta\rho_\delta(p)$. In Figs. 2(b-d) the $\Delta\rho_{-5\Gamma,0,+5\Gamma}(p)$ at $s = 35.8$ after 100- μs interaction (red dash-dot curves) are shown as a comparison to the 200- μs case. Small but clear differences of $\Delta\rho(p)$ are observed for all three detunings indicating that the momentum distribution undergoes some time evolution, which may result in a time-dependent absorption lineshape. This is actually demonstrated in Fig. 3 by comparing the saturation-dependent shift of the absorption peak position for the 100- and 200- μs imaging durations. The peak position is shifted towards the positive detuning when increasing the imaging intensity and such a shift becomes larger in the case of a longer exposure, i.e. more photons are scattered. The solid curves represent the calculated results without any free parameters, while the solid dots are from fits with the peak position and height as the free fitting parameters [see Fig. 2(a)]. Overall, the fitted shifts agree well with the calculations without free parameters, while deviations are seen for some points coming from fluctuations of experimental conditions like laser power and atom number, as well as the low SNR at strong saturations.

V. CONCLUSION

In conclusion, we have presented a simple experiment studying the photon recoil effects in the absorption spectrum of a narrow-line transition with an ultracold strontium gas, where the investigated parameter regime has not been experimentally studied before and a quantitative understanding of the observations is shown by OBEs using the "momentum family" method. Our study can be extended to high-density samples, in which the inter-particle distance is comparable to or smaller than the probe wavelength. Various collective and cooperative effects are predicted theoretically under these conditions [34–37] and atomic motions are essential there. The narrow-line absorption studied here can also be employed as sensitive probes for detection of interaction effects in divalent systems, e.g. the spatial correlation due to Rydberg blockade [38].

ACKNOWLEDGEMENTS

We acknowledge C. Qiao, L. Couturier, I. Nosske and P. Chen for their contributions on setting up the experiment at the early stage of project. F.H acknowledges Yaxiong Liu for helpful discussions on numerical algorithms. We are supported by the Anhui Initiative in Quantum Information Technologies. Y.H.J. also acknowledges support from the National Natural Science Foundation under Grant No. 11827806.

APPENDIX

A. Low-saturation absorption

In Fig. 4, we show two measured absorption spectra at temperatures of $1.3 \mu\text{K}$ (black points) and $5.7 \mu\text{K}$ (red points) with a saturation parameter of $s = 0.1$. The TOF time τ_{TOF} (see Fig. 1(b)) is chosen to be 3.1 ms to minimize the lensing effect (see Appendix B) as well as to keep large enough SNR in the OD images. The plotted signals in Fig. 4 are the OD integrals over the whole atomic cloud region divided by the peak cross section $\sigma_0 = 3\lambda^2/2\pi$.

Symmetric lineshapes are observed in both cases and the linewidth increases with the increasing temperature. The spectra fit well to Voigt profiles with a fixed Lorentzian width of $v_L = 10.01$ kHz, resulted from the power broadening $\Gamma\sqrt{1+s}/2\pi$ and the detection bandwidth $0.9/\tau_{\text{exp}} = 4.5$ kHz due to the finite length of the square-shape imaging pulse (see Fig. 1(b)), where $\Gamma/2\pi = 7.5$ kHz is the natural linewidth. The FWHM Gaussian width v_G obtained from the Voigt profile fitting agrees excellently with the Doppler width deduced from the cloud temperatures.

Other than revealing the temperature information, the atom number and atomic density can also be ex-

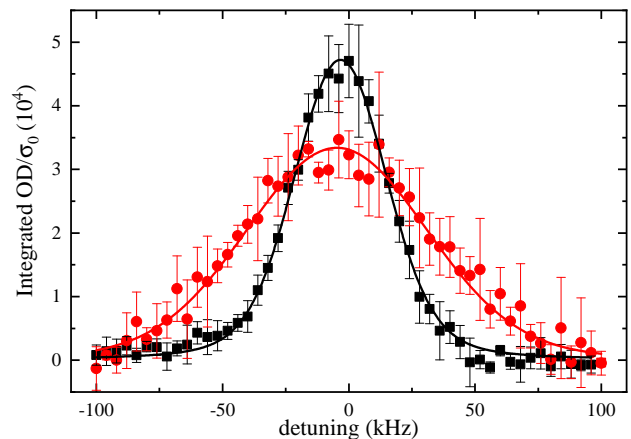


FIG. 4. Low-saturation absorption spectra at temperatures of $1.3 \mu\text{K}$ (black) and $5.7 \mu\text{K}$ (red). The integrated absorption signal over the atomic cloud region is plotted as a function of the imaging detuning. The error bars are standard deviations out of five repeated measurements. The solid curves are fits to the Voigt profile. See text for more details.

tracted from the narrow-linewidth absorption imaging in the low saturation regime. Broad transitions typically used in determining the atom number and atomic density have natural linewidths on the order of 10 MHz, much broader than the Doppler widths in the ultracold regime. The absorption cross-section in the broad-transition imaging can hence be regarded as temperature-independent. However, for the narrow transition with a natural linewidth smaller than the Doppler width ($\Gamma/2\pi v_G < 1$), the Doppler effect has to be considered when calculating the atom number [39]. This is done by convolving the velocity-dependent Lorentzian absorption profile with the Maxwell-Boltzmann velocity distribution in the atomic sample. In general, the low-saturation ($s \ll 1$) OD can be calculated as

$$\begin{aligned}
 OD(x, y) &= \sigma_0 n(x, y) \int_{-\infty}^{+\infty} \frac{1}{u\sqrt{\pi}} e^{-(v/u)^2} \frac{\Gamma^2/4}{(\delta - kv)^2 + \Gamma^2/4} dv \\
 &= \sigma_0 n(x, y) \frac{\alpha^2}{\sqrt{\pi}} \int_{-\infty}^{+\infty} \frac{e^{-(x'+\delta/ku)^2}}{x'^2 + \alpha^2} dx' \\
 &\stackrel{\delta=0}{\equiv} \sigma_0 n(x, y) \times C(\Gamma, v_G),
 \end{aligned} \tag{6}$$

where $C(\Gamma, v_G) = \sqrt{\pi}\alpha e^{\alpha^2} \text{Erfc}(\alpha)$ is a coefficient with $\alpha = \sqrt{\ln 2}\Gamma/2\pi v_G$ when the detuning δ is zero, and $n(x, y)$ is the atomic column density. $\text{Erfc}(x)$ is the complementary error function. With the measured on-resonance OD and the temperature-dependent v_G determined from the spectrum width, the atom number and atomic density can be obtained with Eq. (6).

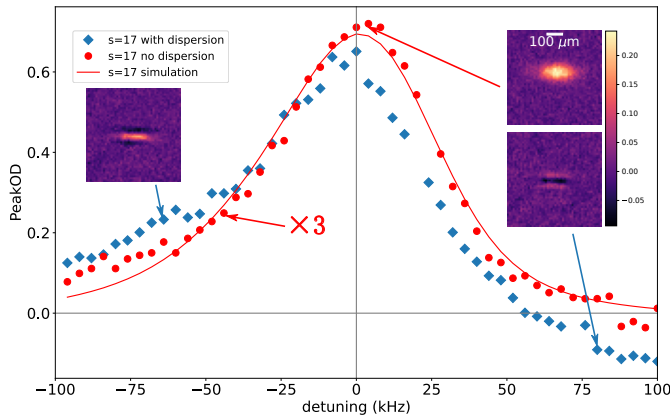


FIG. 5. Absorption spectrum with $s = 17$ at two different atomic densities of $8.9 \times 10^{10} \text{ cm}^{-3}$ (red circles) and $2.8 \times 10^{11} \text{ cm}^{-3}$ (blue diamonds). The red curve is a fit to the numerical solution of Eq. (4). We obtain negative peak ODs at some large positive detunings. In the right inset, the lower OD image measured at a large positive detuning with the high atomic density has a dark hole instead of a bright peak in the cloud center, caused by the lensing effect. At the large negative detuning, the dark position appears at the edges of the cloud (left inset). As a comparison, we also show an example of the OD images for the low-density case with a normal Gaussian distribution in the upper panel of the inset.

B. The lensing effect

As shown in Fig. 5, we have also experimentally observed another phenomenon in the absorption spectrum at high atomic densities, the so-called lensing effect which is well known in standard absorption imaging. The ab-

sorption spectra at two different atomic densities, tuned by τ_{TOF} , are compared at a saturation of $s = 17$. For a better illustration of the lensing, we show the peak OD instead of the integrated one as a function of the detuning. In the low-density case ($\tau_{\text{TOF}} = 3.1 \text{ ms}$, $n \sim 8.9 \times 10^{10} \text{ cm}^{-3}$, red dots in the figure), we find a similar asymmetry as that in Fig. 2(a) for the high saturation. With a 3-fold higher density ($\tau_{\text{TOF}} = 1.1 \text{ ms}$, $n \sim 2.8 \times 10^{11} \text{ cm}^{-3}$, blue diamonds in the figure), a negative peak OD is obtained from the two-dimensional Gaussian fit at some large positive detunings. Checking the OD images there (one example shown as the right inset in Fig. 5), a dark hole instead of a bright peak is seen at the central region of the atomic cloud for the large positive detuning, while at the negative one a dark edge is observed. This phenomenon is related to the microscopic lensing effect studied in e.g. Refs. [40–46], where a spatial-dependent index of refraction leads to a focusing or defocusing effect on the imaging beam depending on the detuning.

The observed lensing effect here mainly stems from the density inhomogeneity as indicated by the density-dependence (see Fig. 5) and the fact that the imaging beam is much larger than the atomic cloud (~ 200 times). The lensing induced by such density inhomogeneity was observed in both the weak- [43] and strong-saturation [40–42] regimes. The lensing effect shown in Fig. 5 with strong saturation is also observable in the weak-probe case in our experiment. However, to quantitatively explain our observation, detailed calculations on the light propagation are needed like in Refs. [44, 46], even including the atom dipolar interactions or multiple scattering events (e.g. [35, 47, 48]), which is beyond the current scope.

-
- [1] Cohen-Tannoudji C 1990 *Fundamental systems in quantum optics* 1–164
 - [2] Kolchenko A, Rautian S and Sokolovskii R 1969 *Sov. Phys. JETP* **28** 986
 - [3] Weiss D S, Young B C and Chu S 1993 *Phys. Rev. Lett.* **70**(18) 2706–2709 URL <https://link.aps.org/doi/10.1103/PhysRevLett.70.2706>
 - [4] Li Q, Xu D Z, Cai C Y and Sun C P 2013 *Scientific Reports* **3** 3144 ISSN 2045-2322 URL <https://www.nature.com/articles/srep03144>
 - [5] Robicheaux F 2019 *Journal of Physics B: Atomic, Molecular and Optical Physics* **52** 244001 ISSN 0953-4075 URL <https://doi.org/10.1088/1361-6455/ab4c22>
 - [6] Shahmoon E, Lukin M D and Yelin S F 2019 *Advances In Atomic, Molecular, and Optical Physics* **68** 1–38
 - [7] Hall J L 1978 *Science* **202** 147–156 ISSN 0036-8075, 1095-9203 URL <https://www.sciencemag.org/lookup/doi/10.1126/science.202.4364.147>
 - [8] Guo J, Berman P R, Dubetsky B and Grynberg G 1992 *Physical Review A* **46** 1426–1437 ISSN 1050-2947, 1094-1622 URL <https://link.aps.org/doi/10.1103/PhysRevA.46.1426>
 - [9] Courtois J Y, Grynberg G, Lounis B and Verkerk P 1994 *Physical Review Letters* **72** 3017–3020 URL <https://link.aps.org/doi/10.1103/PhysRevLett.72.3017>
 - [10] Bonifacio R and De Salvo L 1994 *Nuclear Instruments and Methods in Physics Research Section A: Accelerators, Spectrometers, Detectors and Associated Equipment* **341** 360–362
 - [11] Slama S, Bux S, Krenz G, Zimmermann C and Courteille P W 2007 *Phys. Rev. Lett.* **98**(5) 053603 URL <https://link.aps.org/doi/10.1103/PhysRevLett.98.053603>
 - [12] Hall J L, Bordé C J and Uehara K 1976 *Physical Review Letters* **37** 1339–1342 ISSN 0031-9007 URL <https://link.aps.org/doi/10.1103/PhysRevLett.37.1339>
 - [13] Riehle F, Ishikawa J and Helmcke J 1988 *Physical Review Letters* **61** 2092–2095 URL <https://link.aps.org/doi/10.1103/PhysRevLett.61.2092>
 - [14] Bagayev S N, Baklanov A E, Chebotayev V P and Dyckov A S 1989 *Applied Physics B* **48** 31–35 ISSN 1432-0649 URL <https://doi.org/10.1007/BF00694414>
 - [15] Oates C W, Wilpers G and Hollberg L 2005 *Physical Review A* **71** 023404 URL <https://link.aps.org/doi/10.1103/PhysRevA.71.023404>

- [16] Grimm R and Mlynek J 1988 *Physical Review Letters* **61** 2308–2311
- [17] Grimm R and Mlynek J 1989 *Physical Review Letters* **63** 232–235 URL <https://link.aps.org/doi/10.1103/PhysRevLett.63.232>
- [18] Grimm R and Mlynek J 1989 *Applied Physics B Photo-physics and Laser Chemistry* **49** 179–189
- [19] Grimm R and Mlynek J 1990 *Physical Review A* **42** 2890–2905 URL <https://link.aps.org/doi/10.1103/PhysRevA.42.2890>
- [20] Minardi F, Artoni M, Cancio P, Inguscio M, Giusfredi G and Carusotto I 1999 *Phys. Rev. A* **60**(5) 4164–4167 URL <https://link.aps.org/doi/10.1103/PhysRevA.60.4164>
- [21] Artoni M, Carusotto I and Minardi F 2000 *Phys. Rev. A* **62**(2) 023402 URL <https://link.aps.org/doi/10.1103/PhysRevA.62.023402>
- [22] Zheng X, Sun Y R, Chen J J, Wen J L and Hu S M 2019 *Physical Review A* **99** 032506 URL <https://link.aps.org/doi/10.1103/PhysRevA.99.032506>
- [23] Christensen R S, Levinsen J and Bruun G M 2015 *Physical Review Letters* **115**
- [24] Westergaard P G, Christensen B T, Tieri D, Matin R, Cooper J, Holland M, Ye J and Thomsen J W 2015 *Physical Review Letters* **114**
- [25] Hu J, Urvoy A, Vendeiro Z, Crépel V, Chen W and Vuletić V 2017 *Science* **358** 1078–1080 ISSN 0036-8075, 1095-9203 URL <http://science.sciencemag.org/content/358/6366/1078>
- [26] Hu M G, Liu Y, Grimes D D, Lin Y W, Gheorghe A H, Vexiau R, Bouloufa-Maafa N, Dulieu O, Rosenband T and Ni K K 2019 *Science* **366** 1111–1115 ISSN 0036-8075, 1095-9203 URL <https://science.sciencemag.org/content/366/6469/1111>
- [27] Rudolph J, Wilkason T, Nantel M, Swan H, Holland C M, Jiang Y, Garber B E, Carman S P and Hogan J M 2020 *Physical Review Letters* **124**
- [28] Nosske I, Couturier L, Hu F, Tan C, Qiao C, Blume J, Jiang Y H, Chen P and Weidemüller M 2017 *Physical Review A* **96** 053415 URL <https://link.aps.org/doi/10.1103/PhysRevA.96.053415>
- [29] Qiao C, Tan C Z, Hu F C, Couturier L, Nosske I, Chen P, Jiang Y H, Zhu B and Weidemüller M 2019 *Applied Physics B* **125** 215 ISSN 1432-0649 URL <https://doi.org/10.1007/s00340-019-7328-3>
- [30] Ketterle W, Durfee D S and Stamper-Kurn D M 1999 *arXiv:cond-mat/9904034* Comment: Long review paper with ~90 pages, ~20 figures. 2 GIF figures in separate files (4/5/99 fixed figure) (*Preprint cond-mat/9904034*) URL <http://arxiv.org/abs/cond-mat/9904034>
- [31] Lewandowski H J, Harber D, Whitaker D L and Cornell E A 2003 *Journal of low temperature physics* **132** 309–367
- [32] Stenholm S 1978 *Applied Physics* **15** 287–296
- [33] Castin Y, Wallis H and Dalibard J 1989 *JOSA B* **6** 2046–2057 ISSN 1520-8540 URL <https://www.osapublishing.org/josab/abstract.cfm?uri=josab-6-11-2046>
- [34] Bienaimé T, Bachelard R, Piovella N and Kaiser R 2013 *Fortschritte der Physik* **61** 377–392 URL <https://onlinelibrary.wiley.com/doi/abs/10.1002/prop.201200089>
- [35] Zhu B, Li X, He X, Guo M, Wang F, Vexiau R, Bouloufa-Maafa N, Dulieu O and Wang D 2016 **93** 012508 URL <https://link.aps.org/doi/10.1103/PhysRevA.93.012508>
- [36] Kupriyanov D V, Sokolov I M and Havey M D 2017 *Physics Reports* **671** 1–60 ISSN 0370-1573 URL <http://www.sciencedirect.com/science/article/pii/S0370157316303957>
- [37] Bettles R J, Lee M D, Gardiner S A and Rustekoski J 2020 *Communications Physics* **3** 1–9 ISSN 2399-3650 URL <https://www.nature.com/articles/s42005-020-00404-3>
- [38] Günter G, de Saint-Vincent M R, Schempp H, Hofmann C S, Whitlock S and Weidemüller M 2012 *Physical Review Letters* **108**
- [39] Foot C 2004 *Atomic Physics* (Oxford University Press) ISBN 0198506961 URL https://www.ebook.de/de/product/3611193/c_j_department_of_physics_university_of_oxford_foot_atomic_physics.html
- [40] Labeyrie G, Ackemann T, Klappauf B, Pesch M, Lippi G and Kaiser R 2003 *The European Physical Journal D - Atomic, Molecular, Optical and Plasma Physics* **22** 473–483 ISSN 1434-6079 URL <https://doi.org/10.1140/epjd/e2003-00046-4>
- [41] Wang Y and Saffman M 2004 *Physical Review A* **70** ISSN 1050-2947, 1094-1622 URL <https://link.aps.org/doi/10.1103/PhysRevA.70.013801>
- [42] Labeyrie G, Gattobigio G L, Chanelière T, Lippi G L, Ackemann T and Kaiser R 2007 *The European Physical Journal D* **41** 337–348 ISSN 1434-6079 URL <https://doi.org/10.1140/epjd/e2006-00234-8>
- [43] Roof S, Kemp K, Havey M, Sokolov I M and Kupriyanov D V 2015 *Optics Letters* **40** 1137–1140 ISSN 1539-4794 URL <https://www.osapublishing.org/ol/abstract.cfm?uri=ol-40-7-1137>
- [44] Han J, Vogt T, Manjappa M, Guo R, Kiffner M and Li W 2015 *Physical Review A* **92** 063824 URL <https://link.aps.org/doi/10.1103/PhysRevA.92.063824>
- [45] Noaman M, Langbecker M and Windpassinger P 2018 *Opt. Lett.* **43** 3925–3928 URL <http://ol.osa.org/abstract.cfm?URI=ol-43-16-3925>
- [46] Gilbert J R, Roberts C P and Roberts J L 2018 *Journal of the Optical Society of America B* **35** 718 ISSN 0740-3224, 1520-8540 URL <https://www.osapublishing.org/abstract.cfm?URI=josab-35-4-718>
- [47] Bromley S L, Zhu B, Bishof M, Zhang X, Bothwell T, Schachenmayer J, Nicholson T L, Kaiser R, Yelin S F, Lukin M D, Rey A M and Ye J 2016 *Nature Communications* **7** 11039 ISSN 2041-1723 URL <http://www.nature.com/articles/ncomms11039>
- [48] Chabé J, Rouabah M T, Bellando L, Bienaimé T, Piovella N, Bachelard R and Kaiser R 2014 *Physical Review A* **89** 043833